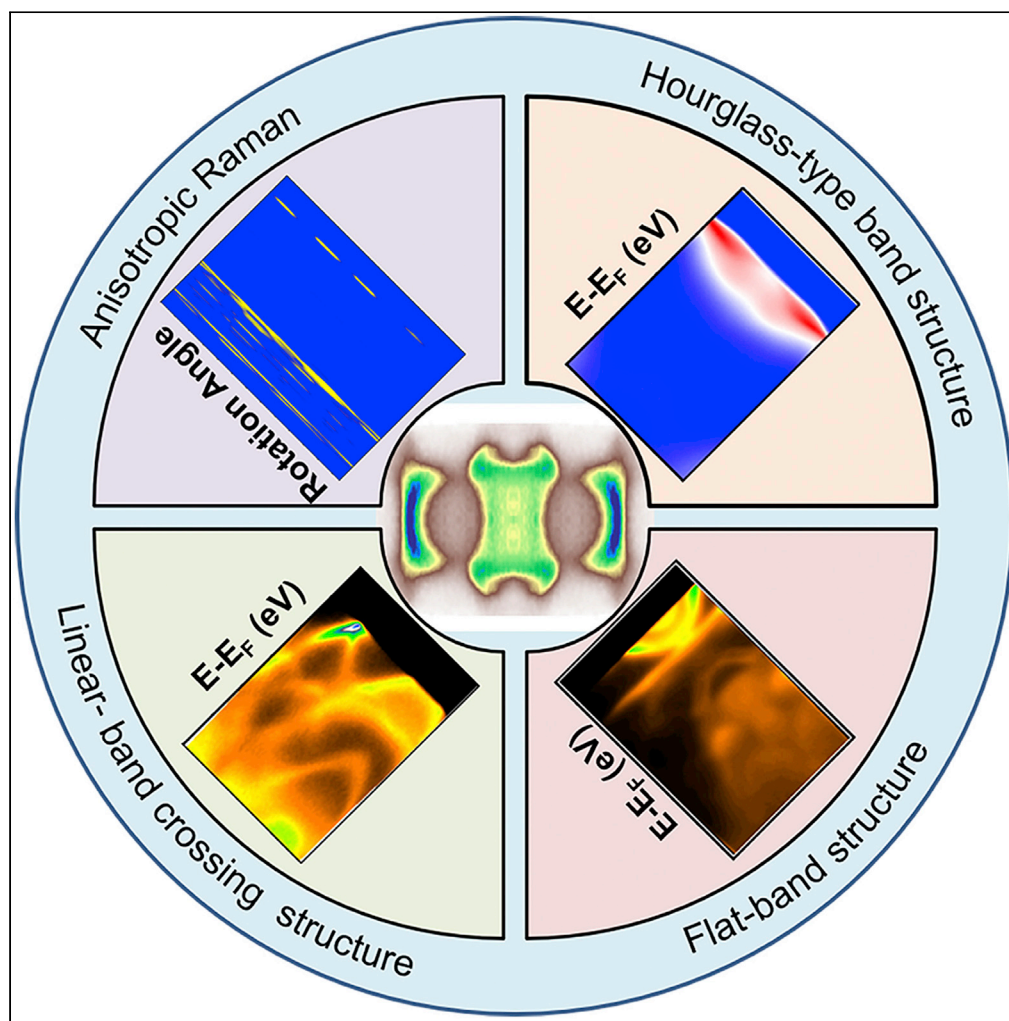Article

Coexistence of the hourglass and nodal-line dispersions in Nb$_3$SiTe$_6$ revealed by ARPES

Zhanfeng Liu, Tongrui Li, Bo Zhang, ..., Shuangming Chen, Zhe Sun, Li Song

song2012@ustc.edu.cn (L.S.)
zsun@ustc.edu.cn (Z.S.)

Highlights

The hourglass-type dispersion is clearly visible from the results of the experiment

Two bulk nodal-lines were found along the S-X and S-R-U high-symmetric directions

The flat band shows the material hosts a quasi-one-dimensional characteristic

Article

Coexistence of the hourglass and nodal-line dispersions in Nb_3SiTe_6 revealed by ARPES

Zhanfeng Liu,[1,5] Tongrui Li,[1,5] Bo Zhang,[1,5] Mukhtar Lawan Adam,[1] Wen Zhu,[1] Yuliang Li,[1] Sheng Wang,[1] Yunbo Wu,[1] Hongen Zhu,[1] Dengfeng Cao,[1] Qilong Cui,[1] Shengtao Cui,[1] Yi Liu,[1] Shuangming Chen,[1] Zhe Sun,[1,2,3,*] and Li Song[1,4,6,*]

SUMMARY

The non-symmorphic crystal symmetry protection in the layered topological semimetal Nb_3SiTe_6 can generate exotic band crossings. Herein, high-quality Nb_3SiTe_6 single crystal was synthesized via chemical vapor transport. The lattice structure of Nb_3SiTe_6 was characterized by scanning transmission electron microscopy, X-ray diffraction, core-level photoemission, and Raman spectroscopies. Angle-resolved photoemission spectroscopy was used to reveal its topological properties by presenting band structures along different high-symmetry directions. Our data show that nontrivial band features coexist in Nb_3SiTe_6, including an hourglass-type dispersion formed by two bands along the S-R high-symmetry line, two node lines along the S-X path and the S-R-U path, respectively. These results provide a context for the understanding and exploration of the exotic topological properties of Nb_3SiTe_6.

INTRODUCTION

Topological semimetals are a class of gapless quantum materials with topologically protected band features. They are currently the frontiers of quantum materials research due to their ability to host exotic electronic states and novel quantum phenomena with unique transport properties and high carrier mobility (Barati and Abedinpour, 2017; Liang et al., 2015; Rhim and Kim, 2016; Schoop et al., 2016; Sun et al., 2017; Xiong et al., 2016). Topological semimetals can be divided into topological Dirac semimetals, Weyl semimetals, node-line semimetals, node-surface semimetals, and so on. Their exotic band crossings are usually protected by specific crystalline symmetries (Fang et al., 2015; Bradlyn et al., 2017; Po et al., 2017; Song et al., 2018; Tang et al., 2019; Watanabe et al., 2018; Young et al., 2012; Zhang et al., 2019). For example, Dirac semimetal is topologically stable in the presence of time-reversal symmetry together with crystal lattice symmetry, such as rotation or reflection (Yang et al., 2017). Weyl semimetal can occur in the absence of any symmetry besides translation (Chan et al., 2016; Huang et al., 2015; Lv et al., 2015; Weng et al., 2016). However, the node-line semimetals have more subtypes, because a line can deform into many different geometries, such as a ring or a knot (Cai et al., 2018; Fang et al., 2016; Kim et al., 2015; Yu et al., 2015). The node line can not only form in the presence of the symmorphic group but also in the non-symmorphic group (Ekahana et al., 2017; Hu et al., 2016; Huang et al., 2017). The non-symmorphic symmetries, which are operations involving translations with fractional lattice parameters, play a crucial role in generating the essential crossings, which could be robust against spin-orbit coupling (SOC) (Bradlyn et al., 2016; Chen et al., 2016; Fang et al., 2016; Li et al., 2018; Liang et al., 2016; Parameswaran et al., 2013; Wang et al., 2017b; Wieder and Kane, 2016; Yang et al., 2017; Young and Kane, 2015; Zhu et al., 2018). Because 157 out of the 230 space groups are non-symmorphic, it is essential to study various topological phases of electronic structures protected by non-symmorphic symmetries. Besides, the non-symmorphic symmetries may give rise to more exotic types of band crossings, such as hourglass dispersions and nodal chains (Cai et al., 2018; Wang et al., 2017a).

Experimentally, the angle-dependent Shubnikov-de Haas oscillations of Nb_3SiTe_6 suggest a two-dimensional Fermi surface with a nontrivial π-Berry phase, indicating it to be a topological semimetal (An et al., 2018). Its unique crystal structure dictates the inherent symmetry elements: the inversion P, two glide mirrors $\tilde{M}_x$ and $\tilde{M}_y$, and one mirror M_z. Moreover, it also has time-reversal symmetry T without magnetic ordering (Li et al., 2018). Because there are various symmetries in the crystal, it becomes important to

[1]National Synchrotron Radiation Laboratory, CAS Center for Excellence in Nanoscience, University of Science and Technology of China, Hefei, Anhui 230029, China

[2]CAS Key Laboratory of Strongly-coupled Quantum Matter Physics, University of Science and Technology of China, Hefei, Anhui 230026, China

[3]Collaborative Innovation Center of Advanced Microstructures, Nanjing 210093, China

[4]State Key Laboratory of Inorganic Synthesis and Preparative Chemistry, College of Chemistry, Jilin University, Changchun 130012, China

[5]These authors contributed equally

[6]Lead contact

*Correspondence: song2012@ustc.edu.cn (L.S.), zsun@ustc.edu.cn (Z.S.)

https://doi.org/10.1016/j.isci.2022.103952

investigate novel properties associated with these symmetries, in particular, the relationship between topological characteristics and symmetries. It has been predicted that, when a crystal hosts different symmetry elements, various topological features may coexist (Cai et al., 2018; Weng et al., 2016; Zhang et al., 2017). Nb_3SiTe_6 has been proposed to host an hourglass-type dispersion and a drumhead-like surface state protected by its non-symmorphic symmetry (Li et al., 2018). Recently, researchers have revealed that Nb_3SiTe_6 is a weak topological insulator with hourglass fermions. However, the existence of hourglass fermions still lacks strong evidence in the experiment. Therefore, it is critical to study such fermions experimentally and explore the exotic band structure comprehensively.

Herein, utilizing the angle-resolved photoemission spectroscopy (ARPES), we have studied electronic structures of Nb_3SiTe_6. Along the S-R direction, a gap exists between the valence band and conduction band being around the Fermi level, highlighting the hourglass-type dispersions of the bulk band structure dictated by its non-symmorphic space group. We also found a nodal line along the S-R-U path at $E-E_F \approx$ -0.5 eV and a node line along the S-X path close to the Fermi level. In addition, a flat band is located at $E-E_F \approx$ -0.25 eV in the Γ-Y direction, suggesting a strong one-dimensional characteristic in this band. These topological features coexist in the layered Nb_3SiTe_6. Our results demonstrated that Nb_3SiTe_6 is a desirable platform to study multiple topological properties.

RESULT AND DISCUSSION

We have successfully grown a high-quality single-crystal Nb_3SiTe_6 through chemical vapor transport. Nb_3SiTe_6 is a van der Waals material with a layered structure. As shown in Figure 1A, a unit cell is formed by three different kinds of building units—two zigzag chains with (Nb-Nb)-(Si) cationic sequences and the $NbTe_2$ chains (Yang et al., 2019; Zhu et al., 2020), belonging to space group No.62 (Pnma). First-principles band calculations (Li et al., 2018) show that when the spin-orbit coupling (SOC) is neglected, Nb_3SiTe_6 displays a fourfold-degenerated (eightfold-degenerate if counting spin) nodal line along the S-R line in the bulk Brillouin zone (BZ) due to the band crossing protected by the glide mirror symmetry. It is also suggested that when the SOC is included, the 4-fold degeneracy is slightly lifted, and as a result, hourglass-like dispersions show up in the close vicinity of E_F. It is highly desirable to experimentally examine electronic structures of Nb_3SiTe_6 to verify theoretical calculations.

Firstly, we investigated the crystal structure of Nb_3SiTe_6 single crystal. The sharp X-ray diffraction peaks prove its high-quality crystallinity (Figure 1B). The scanning transmission electron microscopy (STEM) of Nb_3SiTe_6 in Figure 1C reveals the microstructure of Nb_3SiTe_6. The inset image is the corresponding Fast Fourier Transform pattern, which further confirms the highly crystalline nature of Nb_3SiTe_6 single crystal. In Figure 1D, we show the Te 4d core-level spectrum. The main peaks come from the Nb-Te-Si bond. The shoulder peaks are affected by Te-Nb bond as indicated by arrows, which are intrinsic characteristics of the XPS data for such materials (Yang et al., 2019). In addition, the atomic ratio Nb: Si: Te is close to 3: 1: 6 with uniform element distribution, as determined by energy-dispersive spectroscopy analysis (Figure S1). The specific atom percentage of Nb_3SiTe_6 is shown in Table S1. The Raman measurements are also consistent with previous reports (Hu et al., 2015) (Figure S2). Previous studies on $NbSi_{0.45}Te$ found that different Si contents significantly influence its crystal structure as well as band structures. Our results ensure the accuracy of our sample.

ARPES measurements were performed to visualize the electronic states of Nb_3SiTe_6, with emphasis on the topological band structures protected by crystal symmetry. Because of the non-symmorphic symmetry protection, the characteristic band crossing can stably exist against the action of spin-orbit coupling (Ekahana et al., 2017). In Figure 2A, we show the Brillouin zone of Nb_3SiTe_6. The high-symmetry points are labeled. The Fermi surface probed by ARPES is shown in Figure 2B, and the strong anisotropy is consistent with the transport behavior (Hu et al., 2015). Both cases are determined by the specific crystal structures. Considering that the Raman data (Figure S2) also exhibit clear anisotropy, this material could be of importance in some application (Neupane et al., 2014).

To accurately detect the high-symmetry direction and the high-symmetry plane, we varied photon energies to take ARPES data along the Γ-Z direction. As shown in Figure 2C, the modulation of ARPES intensity enables us to determine the high-symmetry points in momentum space. The Fermi surface of the Γ-X-S-Z plane along the k_z direction is shown in Figure 2D. One can see that the dispersion along the k_z direction is insignificant, suggesting a weak interlayer coupling in Nb_3SiTe_6.
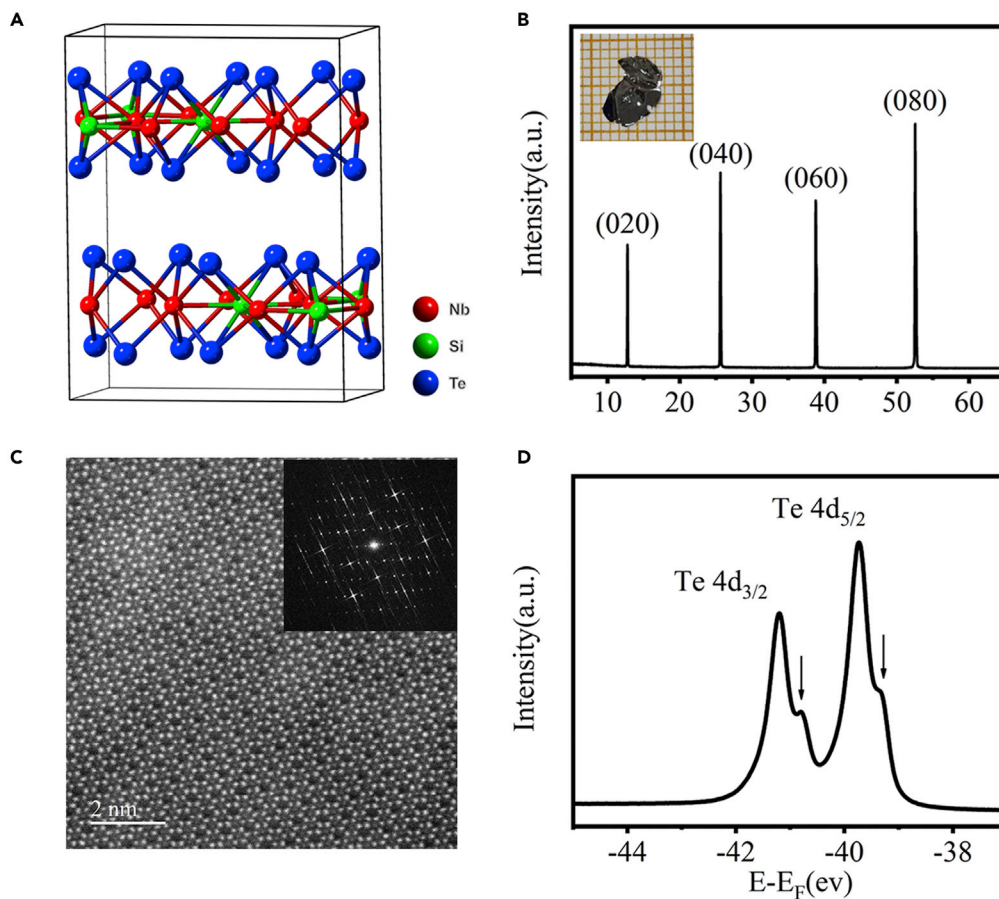
Figure 1. Morphology and characterization of Nb₃SiTe₆

(A) Crystal structure of the Nb_3SiTe_6.

(B) Single-crystal X-ray diffraction data along the (0 k 0) plane, and the inset digital photo exhibits a piece of single crystal.

(C) STEM image with the inset showing the corresponding Fast Fourier Transform pattern.

(D) Photoemission spectra of the core levels of Nb_3SiTe_6 Te 4d levels.

We also searched for the band crossing by selecting k_z. Figure 3A shows the ARPES intensity at the Fermi level along the Z-S-R-T plane ($k_z \sim \pi$). Figures 3B and 3C display the band dispersions along different cuts indicated in Figure 3A. Cuts A–C are in the first Brillouin zone, and Cuts D–E in the second Brillouin zone. The photoemission matrix-element effect has an impact on the intensity of dispersive bands in the first Brillouin zone, so the analysis should combine the data in the second Brillouin zone. Figure 3B shows the ARPES intensity along cut A, corresponding to the S-Z direction. There are two linear band crossings around S high-symmetry point, as indicated by the white arrows in Figure 3B, which is consistent with previous studies of Ta₃SiTe₆ (Sato et al., 2018). However, Cuts C–E are parallel with cut A, showing a variation in the band structure. The linear band crossing disappears and a small gap shows up between the same conduction band and valence band, as indicated by the white arrow. To better present the band structure, we show the second-derivative images of these electronic structures (Figure 3D). As indicated by the white arrows, there is a small gap between the two bands at the R high-symmetry point near the Fermi level. Our data suggest that there is only one node at point S along the S-R path. In addition, our data show that the intersection near E-E_F $\cong$ -0.5 eV from S to R forms a nodal line (NL_SR). This behavior is consistent with previous reports of Ta₃SiTe₆ (Sato et al., 2018).

As described by the first-principles band calculations without spin-orbit coupling (SOC), this material can host a characteristic X-shape Dirac-like dispersion at the S point. These zero-dimensional points are connected on the S-R path to form a 4-fold nodal line (Wan et al., 2021). When SOC is taken into account, the Dirac point will be annihilated, accompanied by the opening of an energy gap, leading to the
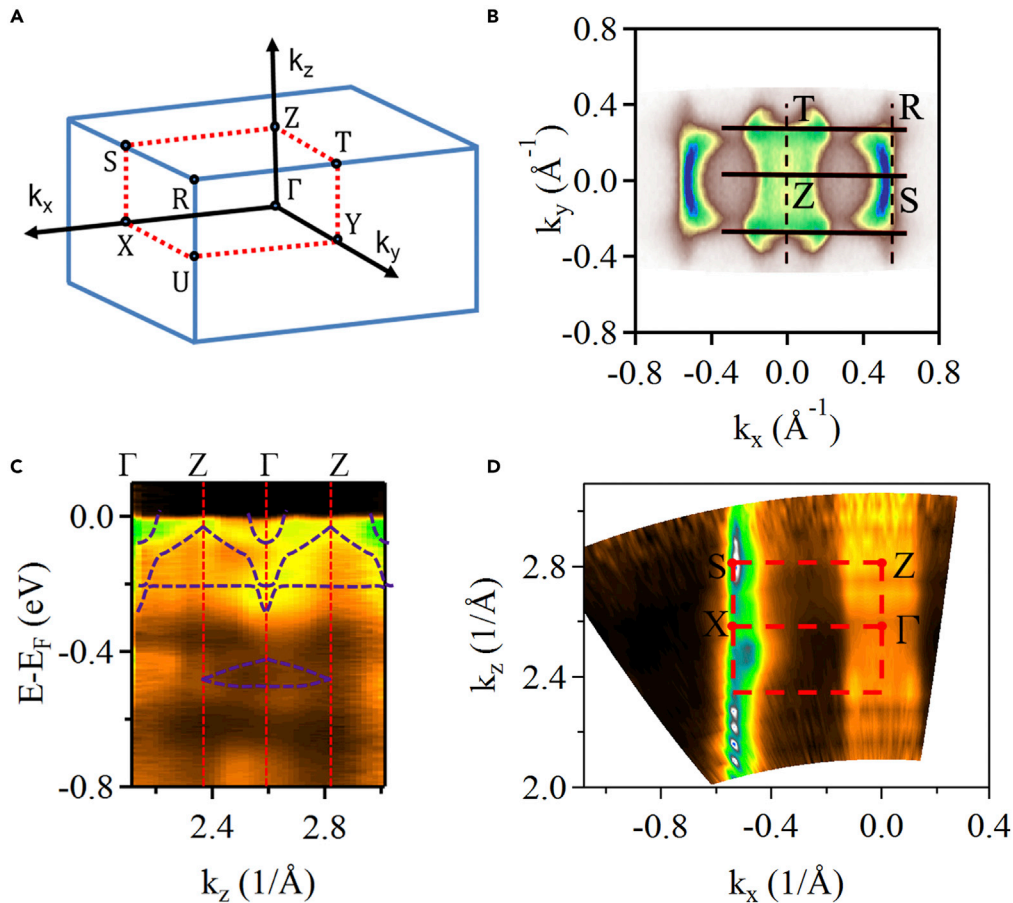
Figure 2. ARPES intensity at Fermi surface along different directions
(A) Bulk orthorhombic Brillouin zone of Nb_3SiTe_6. The high-symmetry points are labeled.
(B) ARPES intensity at E_F plotted as a function of in-plane wave vectors (k_x and k_y) measured at $hv = 15 eV$.
(C) ARPES intensity plot as a function of k_z.
(D) ARPES intensity at E_F plotted as a function of in-plane wave vectors (k_x and k_z).

disappearance of the nodal line that is related to an hourglass-type dispersion (Li et al., 2018; Sato et al., 2018). As shown in Figure 3D, the existence of gap is consistent with hourglass-type dispersion as predicted by band calculations. Figures 3E and 3F show the experimental results and the corresponding second-derivative image of band dispersions along the S-R path. These data are consistent with DFT calculations with SOC along the S-R direction shown in Figure 3G. As indicated by band calculations, there are four individual bands, the two at the top pass through the Fermi level at the S high-symmetry point, and the other two bands exhibit a "glasses-like" structure under the Fermi level. These bands are very close to each other in the energy scale, and the broadening of the bands in ARPES measurements makes it difficult to clearly resolve the hourglass-type dispersion. The second-derivative image in Figure 3F agrees with the calculation in Figure 3G, and the band splitting observed here is consistent with the theoretical calculations of the hourglass-type dispersion. This provides the supporting data for the existence of hourglass fermions.

Furthermore, we surveyed the band structures along other high-symmetry lines in search of exotic fermions. By tuning the incident photon energies, we found band crossings at the S(X) point with different k_z, which form a node line (NL_{SX}) along the S-X direction (Figures 4A and 4B). The detailed Γ-X direction plot with different photon energies are shown in the Figure S3, and one can notice the variation of band dispersion with k_z. Our calculated results are in agreement with the experimental data (Figure 4C). For ARPES measurements with various photon energies, the dispersions of surface states remain the same due to the absence of the k_z dispersion, while the k_z dispersion is usually evident for the bulk states. The previous studies presented the spin-polarized topological surface states with spin-momentum locking in Nb_3XTe_6
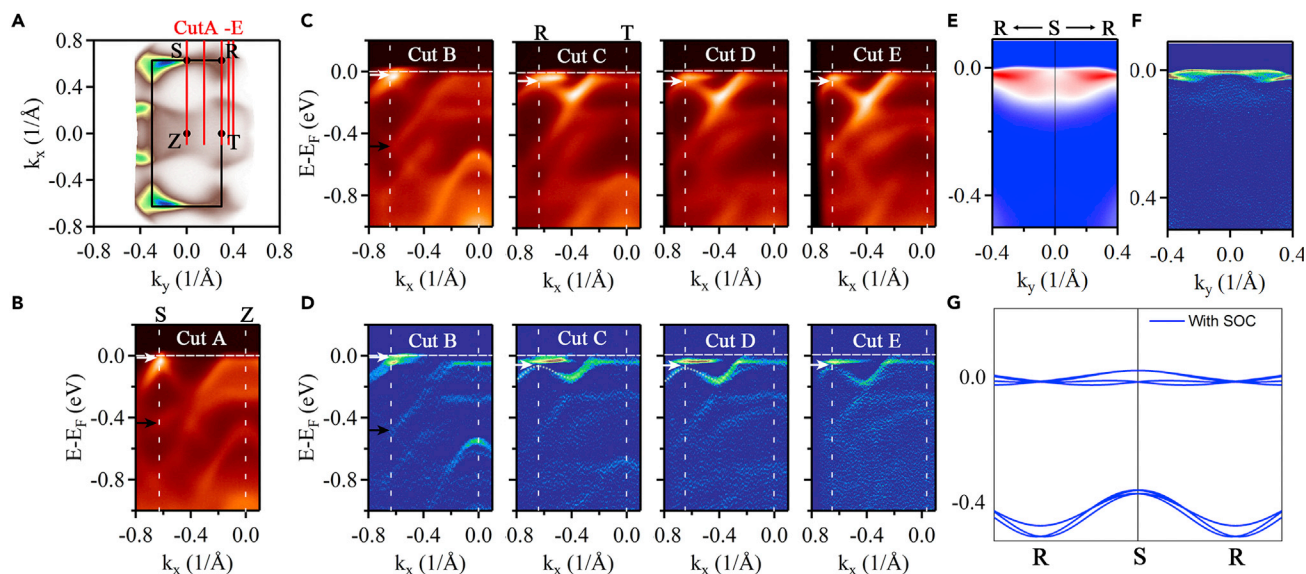
Figure 3. Hourglass-type band structure of single-crystal Nb₃SiTe₆

(A) ARPES intensity distribution at E_F on the $k_z \sim \pi$ plane.

(B) Band dispersion along the Cut A direction in (A).

(C and D) are the electronic structures and the corresponding second-derivative data obtained from the cuts (B–E) in (A).

(E and F) are the ARPES intensity and second-derivative intensity in the vicinity of E_F, respectively, measured along the S-R high symmetry direction.

(G) Calculated band dispersions along S-R with SOC.

around X point (Wan et al., 2021). However, based on our ARPES data, we argue that the NL_{SX} is of bulk states. Interestingly, this node-line is protected by non-symmorphic symmetries, owing to the selection rule related to $\tilde{M}_y$. Also, at the $k_y \sim \pi$ plane, we found a new nodal line along the R-U line (NL_{RU}). Figures 4D and 4E display the plots of the ARPES intensity along the U-Y and R-T high-symmetry lines, respectively. Figure 4F shows band calculations along the T-R-T path. The X-shaped band crossing is distinctly presented as indicated by the arrows in Figures 4D and 4E. In Figures S4 and S5, we showed k_z dependence along the U-Y direction and the energy distribution curves (EDC) along the high-symmetry cut. In our data, the X-shaped Dirac band dispersion is robust, suggesting that Nb₃SiTe₆ hosts a node line along the direction of R-U. This nodal line NL_{RU} is located at $E-E_F \approx$ -0.5 eV. As shown above in Figure 2, the nodal line NL_{SR} on S-R high symmetry at $E-E_F \approx$ -0.5 eV. These two nodal lines are connected at high-symmetry point S to form a longer nodal line (NL_{SRU}) on the S-R-U path. In the presence of space-time inversion symmetry, this node-line is 4-fold degenerated Dirac-like node line.

We further examined the band structures along the Γ-Y. Figures 5A and 5B show two representative cuts along the Γ-Y and Z-T directions. Figures 5C and 5D show the corresponding second-derivative images. There are two conduction bands (α, β) that cross the E_F in the first Brillouin zone. According to the periodicity of the lattice structure, α and β bands should also have large spectral weights in the second Brillouin zone. However, they show weak spectral weight in the second zone due to the selection rule related to $\tilde{M}_x$ (Wan et al., 2021). Figure 5E shows the band calculations of bulk crystal along the Γ-Y, which is consistent with our ARPES data. More interestingly, there exists one flat band (γ) located at -0.25 eV, suggesting a strong one-dimensional characteristic possessed by these electronic states. The calculations of both surface and bulk states are shown in Figure 5F. A new flat band dominated by surface states shows up above the one derived from bulk states. To further illustrate the contribution of individual elements to the flat band, we have calculated band structures projected onto different elements' orbital and electronic density of states, as shown in Figure S6. It reveals that Nb d orbital states contribute the most, followed by Te p orbital states, and Si has almost no contribution. The flat band has a high density of electronic states, strong electronic correlation, etc. Potential applications of topological phase transitions and topological electronic devices can be further investigated using external fields and stresses. Nb₃SiTe₆ produces a variety of topological band structures and provide us with an excellent platform for research in topological properties.
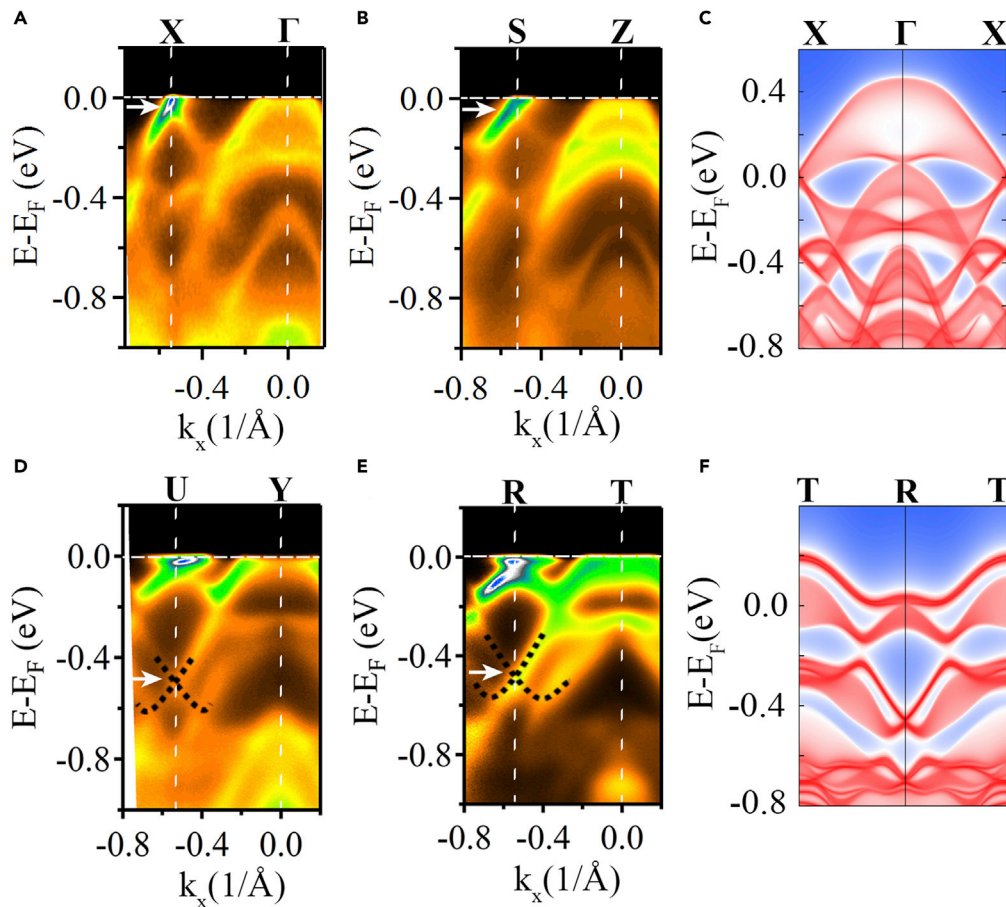
Figure 4. Node-line band structure of single-crystal Nb$_3$SiTe$_6$

(A and B) ARPES intensity plots along the Γ-X and S-Z directions, respectively.

(C and D) ARPES intensity plots along the U-Y and R-T directions, respectively.

(E) The calculations of surface states and bulk states along the Γ-X direction. SOC is not taken into account.

(F) The calculations of surface states and bulk states along the R-T direction. SOC is not taken into account.

CONCLUSION

In summary, high-resolution ARPES data of Nb$_3$SiTe$_6$ revealed the details of band structures along the S-R line, supporting the existence of hourglass-type dispersions protected by the non-symmorphic symmetry, being consistent with the first-principles calculations. The existence of two nodal lines along the high-symmetry S-X and S-R-U path was also demonstrated, respectively. This work highlights that Nb$_3$SiTe$_6$ can be a new type of topological semimetal with several topological electronic states coexisting. Thus, such 2D single-crystals may be an excellent platform to search for novel physical properties induced by the coexistence of multiple topological behaviors.

Limitations of the study

At present, the combination of ARPES measurements and theoretical band calculation has become an important approach. Although we can make qualitative analysis and conclusions, the limited energy resolution of the ARPES technique smears out the details of band dispersions to some extent, though the overall band structures are highly consistent with band calculations.

STAR★METHODS

Detailed methods are provided in the online version of this paper and include the following:
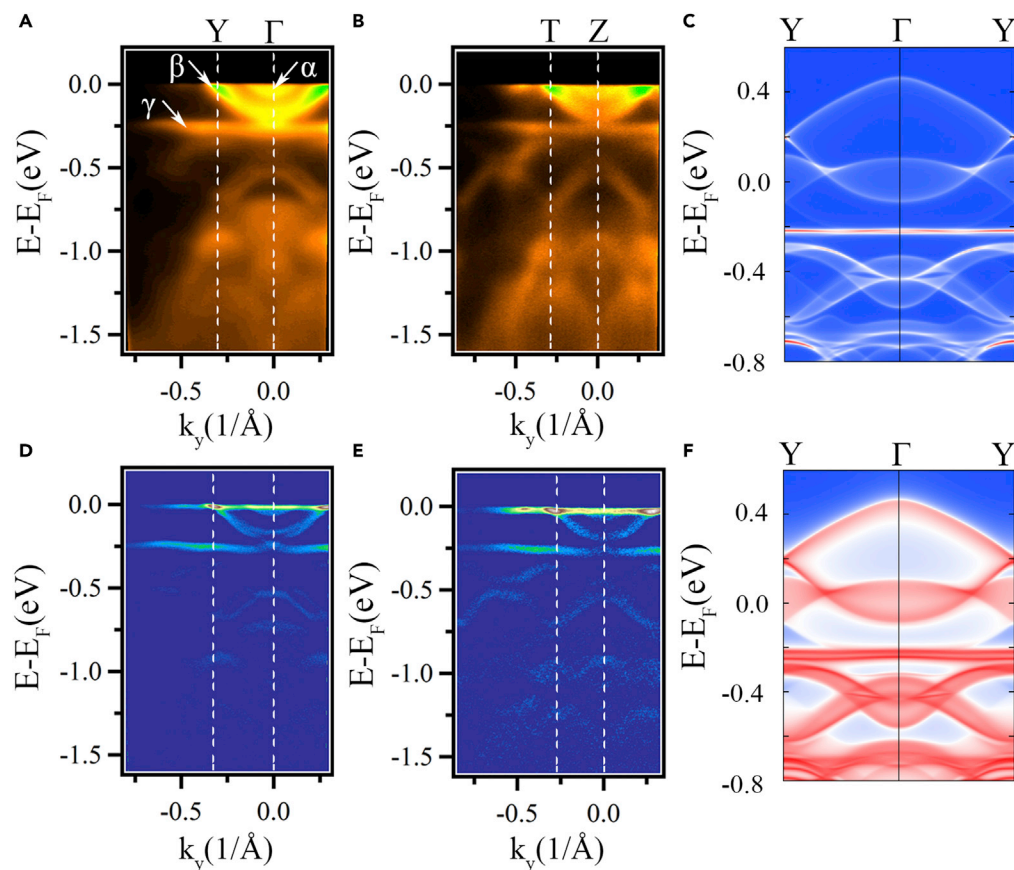
- ● KEY RESOURCES TABLE

Figure 5. Comparison of experience and calculation results along Γ-Y direction

(A) ARPES intensity plot along the Γ-Y direction.

(B) ARPES intensity plot along the T-Z direction.

(C) The calculations of bulk states along the Γ-Y direction.

(D) The second-derivative intensity plot of (A).

(E) The second-derivative intensity plot of (B).

(F) The calculations of surface states and bulk states along the Γ-Y direction. The red lines show the surface states.

- RESOURCE AVAILABILITY
  - Lead contact
  - Materials availability
  - Data and code availability
- EXPERIMENTAL MODEL AND SUBJECT DETAILS
- METHOD DETAILS
  - Sample preparation
  - Computational details
- QUANTIFICATION AND STATISTICAL ANALYSIS
  - Additional resources

SUPPLEMENTAL INFORMATION

Supplemental information can be found online at https://doi.org/10.1016/j.isci.2022.103952.

AUTHOR CONTRIBUTIONS

DECLARATION OF INTEREST

The authors declare no competing interests.

REFERENCES

Ganose, A.M., Jackson, A.J., and Scanlon, D.O. (2018). sumo: command-line tools for plotting and analysis of periodic ab initio calculations. J. Open Source Softw. *3*, 717.

An, L., Zhang, H., Hu, J., Zhu, X., Gao, W., Zhang, J., Xi, C., Ning, W., Mao, Z., and Tian, M. (2018). Magnetoresistance and Shubnikov–de Haas oscillations in layered Nb_3SiTe_6 thin flakes. Phys. Rev. B *97*, 235133.

Barati, S., and Abedinpour, S.H. (2017). Optical conductivity of three and two dimensional topological nodal-line semimetals. Phys. Rev. B *96*, 155150.

Blöchl, P.E. (1994). Projector augmented-wave method. Phys. Rev. B *50*, 17953–17979.

Bradlyn, B., Cano, J., Wang, Z., Vergniory, M.G., Felser, C., Cava, R.J., and Bernevig, B.A. (2016). Beyond Dirac and Weyl fermions: unconventional quasiparticles in conventional crystals. Science *353*, aaf5037.

Bradlyn, B., Elcoro, L., Cano, J., Vergniory, M.G., Wang, Z., Felser, C., Aroyo, M.I., and Bernevig, B.A. (2017). Topological quantum chemistry. Nature *547*, 298–305.

Cai, J., Xie, Y., Chang, P.-Y., Kim, H.-S., and Chen, Y. (2018). Nodal-chain network, intersecting nodal rings and triple points coexisting in nonsymmorphic Ba_3Si_4. Phys. Chem. Chem. Phys. *20*, 21177–21183.

Chan, Y.H., Chiu, C.-K., Chou, M.Y., and Schnyder, A.P. (2016). Ca_3P_2 and other topological semimetals with line nodes and drumhead surface states. Phys. Rev. B *93*, 205132.

Chen, Y., Kim, H.-S., and Kee, H.-Y. (2016). Topological crystalline semimetals in nonsymmorphic lattices. Phys. Rev. B *93*, 155140.

Ekahana, S.A., Wu, S.-C., Jiang, J., Okawa, K., Prabhakaran, D., Hwang, C.-C., Mo, S.-K.,

Sasagawa, T., Felser, C., Yan, B., et al. (2017). Observation of nodal line in non-symmorphic topological semimetal InBi. New J. Phys. *19*, 065007.

Fang, C., Chen, Y., Kee, H.-Y., and Fu, L. (2015). Topological nodal line semimetals with and without spin-orbital coupling. Phys. Rev. B *92*, 081201.

Fang, C., Weng, H., Dai, X., and Fang, Z. (2016). Topological nodal line semimetals. Chin. Phys. B *25*, 117106.

Grimme, S., Antony, J., Ehrlich, S., and Krieg, H. (2010). A consistent and accurate ab initio parametrization of density functional dispersion correction (DFT-D) for the 94 elements H-Pu. J. Chem. Phys. *132*, 154104.

Hu, J., Liu, X., Yue, C.L., Liu, J.Y., Zhu, H.W., He, J.B., Wei, J., Mao, Z.Q., Antipina, L.Y., Popov, Z.I., et al. (2015). Enhanced electron coherence in atomically thin Nb_3SiTe_6. Nat. Phys. *11*, 471–476.

Hu, J., Tang, Z., Liu, J., Liu, X., Zhu, Y., Graf, D., Myhro, K., Tran, S., Lau, C.N., Wei, J., and Mao, Z. (2016). Evidence of topological nodal-line fermions in ZrSiSe and ZrSiTe. Phys. Rev. Lett. *117*, 016602.

Huang, H., Jin, K.-H., and Liu, F. (2017). Topological nodal-line semimetal in nonsymmorphic *Cmce*-phase Ag_2S. Phys. Rev. B *96*, 115106.

Huang, S.-M., Xu, S.-Y., Belopolski, I., Lee, C.-C., Chang, G., Wang, B., Alidoust, N., Bian, G., Neupane, M., Zhang, C., et al. (2015). A Weyl Fermion semimetal with surface Fermi arcs in the transition metal monopnictide TaAs class. Nat. Commun. *6*, 7373.

Kim, Y., Wieder, B.J., Kane, C.L., and Rappe, A.M. (2015). Dirac line nodes in inversion-symmetric crystals. Phys. Rev. Lett. *115*, 036806.

Kresse, G., and Furthmüller, J. (1996). Efficient iterative schemes for ab initio total-energy calculations using a plane-wave basis set. Phys. Rev. B *54*, 11169–11186.

Li, S., Liu, Y., Wang, S.-S., Yu, Z.-M., Guan, S., Sheng, X.-L., Yao, Y., and Yang, S.A. (2018). Nonsymmorphic-symmetry-protected hourglass Dirac loop, nodal line, and Dirac point in bulk and monolayer X_3SiTe_6(X = Ta, Nb). Phys. Rev. B *97*, 045131.

Liang, Q.-F., Zhou, J., Yu, R., Wang, Z., and Weng, H. (2016). Node-surface and node-line fermions from nonsymmorphic lattice symmetries. Phys. Rev. B *93*, 085427.

Liang, T., Gibson, Q., Ali, M.N., Liu, M., Cava, R.J., and Ong, N.P. (2015). Ultrahigh mobility and giant magnetoresistance in the Dirac semimetal Cd_3As_2. Nat. Mater. *14*, 280–284.

Lv, B.Q., Xu, N., Weng, H.M., Ma, J.Z., Richard, P., Huang, X.C., Zhao, L.X., Chen, G.F., Matt, C.E., Bisti, F., et al. (2015). Observation of Weyl nodes in TaAs. Nat. Phys. *11*, 724–727.

Mostofi, A.A., Yates, J.R., Pizzi, G., Lee, Y.-S., Souza, I., Vanderbilt, D., and Marzari, N. (2014). An updated version of wannier90: a tool for obtaining maximally-localised Wannier functions. Comput. Phys. Commun. *185*, 2309–2310.

Neupane, M., Xu, S.-Y., Sankar, R., Alidoust, N., Bian, G., Liu, C., Belopolski, I., Chang, T.-R., Jeng, H.-T., Lin, H., et al. (2014). Observation of a three-dimensional topological Dirac semimetal phase in high-mobility Cd_3As_2. Nat. Commun. *5*, 3786.

Parameswaran, S.A., Turner, A.M., Arovas, D.P., and Vishwanath, A. (2013). Topological order and absence of band insulators at integer filling in non-symmorphic crystals. Nat. Phys. *9*, 299–303.

Perdew, J.P., Burke, K., and Ernzerhof, M. (1996). Generalized gradient approximation made simple. Phys. Rev. Lett. *77*, 3865–3868.

Po, H.C., Vishwanath, A., and Watanabe, H. (2017). Symmetry-based indicators of band topology in the 230 space groups. Nat. Commun. *8*, 50.

Rhim, J.-W., and Kim, Y.B. (2016). Anisotropic density fluctuations, plasmons, and Friedel oscillations in nodal line semimetal. New J. Phys. *18*, 043010.

Sato, T., Wang, Z., Nakayama, K., Souma, S., Takane, D., Nakata, Y., Iwasawa, H., Cacho, C., Kim, T., Takahashi, T., and Ando, Y. (2018). Observation of band crossings protected by nonsymmorphic symmetry in the layered ternary telluride Ta_3SiTe_6. Phys. Rev. B *98*, 121111.

Schoop, L.M., Ali, M.N., Straßer, C., Topp, A., Varykhalov, A., Marchenko, D., Duppel, V., Parkin, S.S.P., Lotsch, B.V., and Ast, C.R. (2016). Dirac cone protected by non-symmorphic symmetry and three-dimensional Dirac line node in ZrSiS. Nat. Commun. *7*, 11696.

Song, Z., Zhang, T., Fang, Z., and Fang, C. (2018). Quantitative mappings between symmetry and topology in solids. Nat. Commun. *9*, 3530.

Sun, Y., Zhang, Y., Liu, C.-X., Felser, C., and Yan, B. (2017). Dirac nodal lines and induced spin Hall effect in metallic rutile oxides. Phys. Rev. B *95*, 235104.

Tang, F., Po, H.C., Vishwanath, A., and Wan, X. (2019). Topological materials discovery by large-order symmetry indicators. Sci. Adv. *5*, eaau8725.

Wan, Q., Yang, T.Y., Li, S., Yang, M., Zhu, Z., Wu, C.L., Peng, C., Mo, S.K., Wu, W., Chen, Z.H., et al. (2021). Inherited weak topological insulator signatures in the topological hourglass

semimetal Nb_3XTe_6 (X=Si, Ge). Phys. Rev. B *103*, 165107.

Wang, L., Jian, S.-K., and Yao, H. (2017a). Hourglass semimetals with nonsymmorphic symmetries in three dimensions. Phys. Rev. B *96*, 075110.

Wang, S.-S., Liu, Y., Yu, Z.-M., Sheng, X.-L., and Yang, S.A. (2017b). Hourglass Dirac chain metal in rhenium dioxide. Nat. Commun. *8*, 1844.

Watanabe, H., Po, H.C., and Vishwanath, A. (2018). Structure and topology of band structures in the 1651 magnetic space groups. Sci. Adv. *4*, eaat8685.

Weng, H., Fang, C., Fang, Z., and Dai, X. (2016). Coexistence of Weyl fermion and massless triply degenerate nodal points. Phys. Rev. B *94*, 165201.

Wieder, B.J., and Kane, C.L. (2016). Spin-orbit semimetals in the layer groups. Phys. Rev. B *94*, 155108.

Wu, Q., Zhang, S., Song, H.-F., Troyer, M., and Soluyanov, A.A. (2018). WannierTools: an open-source software package for novel topological materials. Comput. Phys. Commun. *224*, 405–416.

Xiong, J., Kushwaha, S., Krizan, J., Liang, T., Cava, R.J., and Ong, N.P. (2016). Anomalous conductivity tensor in the Dirac semimetal Na_3Bi. EPL *114*, 27002.

Yang, B.-J., Bojesen, T.A., Morimoto, T., and Furusaki, A. (2017). Topological semimetals protected by off-centered symmetries in nonsymmorphic crystals. Phys. Rev. B *95*, 075135.

Yang, T.Y., Wan, Q., Yan, D.Y., Zhu, Z., Wang, Z.W., Peng, C., Huang, Y.B., Yu, R., Hu, J., Mao,

Z.Q., et al. (2019). Directional massless Dirac fermions in a layered van der Waals material with one-dimensional long-range order. Nat. Mater. *19*, 27–33.

Young, S.M., and Kane, C.L. (2015). Dirac semimetals in two dimensions. Phys. Rev. Lett. *115*, 126803.

Young, S.M., Zaheer, S., Teo, J.C.Y., Kane, C.L., Mele, E.J., and Rappe, A.M. (2012). Dirac semimetal in three dimensions. Phys. Rev. Lett. *108*, 140405.

Yu, R., Weng, H., Fang, Z., Dai, X., and Hu, X. (2015). Topological node-line semimetal and Dirac semimetal state in antiperovskite Cu_3PdN. Phys. Rev. Lett. *115*, 036807.

Zhang, T., Jiang, Y., Song, Z., Huang, H., He, Y., Fang, Z., Weng, H., and Fang, C. (2019). Catalogue of topological electronic materials. Nature *566*, 475–479.

Zhang, X., Yu, Z.-M., Sheng, X.-L., Yang, H.Y., and Yang, S.A. (2017). Coexistence of four-band nodal rings and triply degenerate nodal points in centrosymmetric metal diborides. Phys. Rev. B *95*, 235116.

Zhu, Z., Chang, T.-R., Huang, C.-Y., Pan, H., Nie, X.-A., Wang, X.-Z., Jin, Z.-T., Xu, S.-Y., Huang, S.-M., Guan, D.-D., et al. (2018). Quasiparticle interference and nonsymmorphic effect on a floating band surface state of ZrSiSe. Nat. Commun. *9*, 4153.

Zhu, Z., Li, S., Yang, M., Nie, X.-A., Xu, H.-K., Yang, X., Guan, D.-D., Wang, S., Li, Y.-Y., Liu, C., et al. (2020). A tunable and unidirectional one-dimensional electronic system $Nb_{2n+1}SinTe_{4n+2}$. NPJ Quantum Materials 5, 35. https://doi.org/10.1038/s41535-020-0238-0.

STAR★METHODS

KEY RESOURCES TABLE

REAGENT or RESOURCE	SOURCE	IDENTIFIER
Chemicals, peptides, and recombinant proteins		
Niobium powder	aladdin	CAS: 7440-03-1
Silicon Powder	aladdin	CAS: 7440-21-3
Tellurium Powder	aladdin	CAS: 13494-80-9
Tellurium tetrachloride	aladdin	CAS: 10026-07-0
Software and algorithms		
Origin 2018	Originlab	https://www.originlab.com/
Igor pro 6.37	WaveMetrics	https://www.wavemetrics.com/

RESOURCE AVAILABILITY

Lead contact

Further information and requests for resources and reagents should be directed to and will be fulfilled by the Lead Contact, Li Song (song2012@ustc.edu.cn)

Materials availability

This study did not generate new unique reagents.

Data and code availability

- Data reported in this paper will be shared by the lead contact upon request.

- This paper does not report original codes.

- Any additional information required to reanalyze the data reported in this paper is available from the lead contact upon request.

EXPERIMENTAL MODEL AND SUBJECT DETAILS

Our study does not use experimental models typical in the life sciences.

METHOD DETAILS

Sample preparation

High-quality singe-crystal of Nb_3SiTe_6 were grown by the chemical vapor transport method with $TeCl_4$ as the transport agent. High-purity powders of Nb (99.99%), Si (99.99%), and Te (99.99%) were sealed in an evacuated quartz tube, which was subsequently put in a two-zone tube furnace. The temperatures in the furnace set to be 1050°C (source side) and 950°C (sink side), which were kept for 5 days. ARPES measurements were performed at ARPES beamline (BL-13U) of National Synchrotron Radiation Laboratory, Hefei, with DA30 analyzer. The energy and angular resolutions are better than 20 meV and 0.3°, respectively. Single crystals of Nb_3SiTe_6 was cleaved in ultrahigh vacuum better than 7×10^{-11} Torr to achieve clean surfaces.

Computational details

The first-principles based on density functional theory calculations were performed the VASP(Vienna Ab initio Simulation Package) (Kresse and Furthmüller, 1996), using the projector augmented wave(PAW) method (Blöchl, 1994) and the plane-wave basis with an energy cutoff of 450 eV,with generalized gradient approximation of the Perdew Burke Ernzerhof (PBE) (Perdew et al., 1996) for the exchange-correlation functional. Van der Waals corrections were included by the DFT-D3 (Grimme et al., 2010) method when studying structures optimize. The energy and force convergence criteria were set to 10^{-7} eV and 0.02 eV/Å, respectively. And Monkhorst-Pack k-mesh in the first Brillouin zone of 8 × 4 × 4 without soc was used, and when

considering soc the k-mesh of 6 × 3 × 3 was used. We also used the wannier90 (Mostofi et al., 2014) code to obtain the materials' maximally localized functions, we selected the d orbitals of Nb, p orbitals of Si and p orbitals of Te, then p orbitals of Te by using the post-processing code (Ganose et al., 2018). Surface Green's function was used as implemented in WannierTools (Wu et al., 2018) package to calculate the surface states dispersion.

QUANTIFICATION AND STATISTICAL ANALYSIS

Our study does not include statistical analysis or quantification.

Additional resources

Our study has not generated or contributed to a new website/forum or if it is not part of a clinical trial.